

VISUALIZING COALITION FORMATION: FROM HEDONIC GAMES TO IMAGE SEGMENTATION

Pedro H. de Paula França
UFRJ
pedro.franca@ufrj.br

Lucas Lopes Felipe
UFRJ
lucaslopesf2@gmail.com

Daniel Sadoc Menasché
UFRJ
sadoc@ic.ufrj.br

ABSTRACT

We propose image segmentation as a visual diagnostic testbed for coalition formation in hedonic games. Modeling pixels as agents on a graph, we study how a granularity parameter shapes equilibrium fragmentation and boundary structure. On the Weizmann single-object benchmark, we relate multi-coalition equilibria to binary protocols by measuring whether the converged coalitions overlap with a foreground ground-truth. We observe transitions from cohesive to fragmented yet recoverable equilibria, and finally to intrinsic failure under excessive fragmentation. Our core contribution links multi-agent systems with image segmentation by quantifying the impact of mechanism design parameters on equilibrium structures.

1 INTRODUCTION

Coalition formation is a common emergent behavior in multi-agent systems and mechanism design: agents optimize individual utilities under interaction constraints, and equilibria appear as partitions of the population (Bogomolnaia and Jackson, 2002). We leverage intuitive image segmentation to interpret a multi-agent coalition mechanism, providing a quantitative measure of a resolution parameter that controls coalition granularity. Image segmentation is an essential task across a range of scientific and technological domains (Mittal et al., 2022).

The *resolution* parameter γ modulates coalition granularity (Traag et al., 2011), fundamentally reshaping the equilibrium structure of the system (Felipe et al., 2025). By adjusting γ , the system can span the full spectrum of partitions, ranging from a single grand coalition as $\gamma \rightarrow 0$ to a set of individual singletons as $\gamma \rightarrow 1$. Figure 1 illustrates how image segmentation visualizes this transition from smaller to larger values of γ (Fig. 1(b) to Fig. 1(f)), mapping different partition equilibria to varying levels of spatial granularity. Indeed, a central challenge for mechanism designers is identifying the specific value of γ that yields meaningful equilibria for a given real-world application.

We bridge image segmentation and the proposed coalition mechanism by representing the image as a graph where pixels act as nodes. In this framework, the primary distinction between methods lies in the edge construction, which encodes pairwise similarities according to specific schemes (Shi and Malik, 1997; Galun et al., 2003; Alpert et al., 2007). This formulation effectively casts the segmentation task as a network clustering or community detection problem (Avrachenkov et al., 2018).

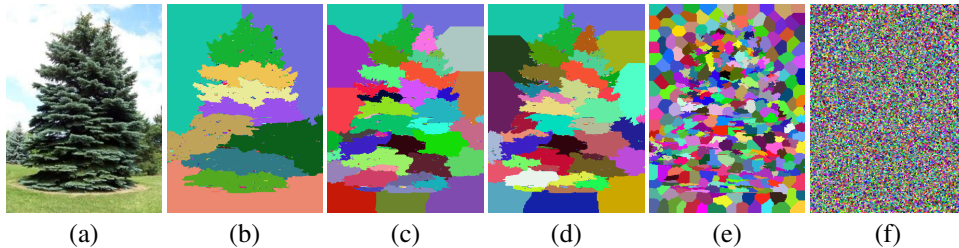


Figure 1: Segmentation of the same image for increasing values of γ . (a) Original image. (b) $\gamma = 10^{-6}$. (c) $\gamma = 8 \times 10^{-6}$. (d) $\gamma = 10^{-5}$. (e) $\gamma = 5 \times 10^{-4}$. (f) $\gamma = 2.5 \times 10^{-1}$.

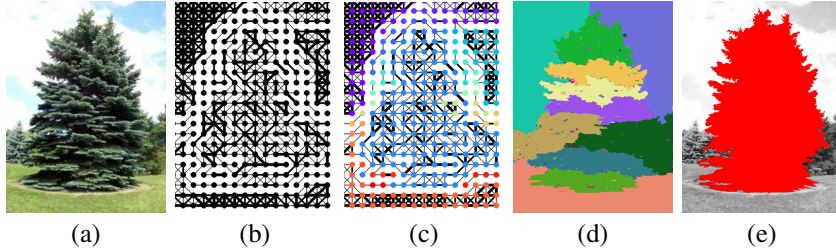


Figure 2: Pipeline: (a) image \rightarrow (b) graph construction (downsampled,¹ see Appendix A) \rightarrow (c) equilibrium partition (Section 2) \rightarrow (d) segmented image \rightarrow (e) ground truth evaluation (Section 3).

Our key contribution lies in using the pipeline in Figure 2 to bridge the gap between multi-agent systems and intuitive image segmentation tasks, so as to quantify the impact of the resolution parameter on equilibrium structures. At the core of the pipeline lies the coalition mechanism (Figure 2(c)), which determines the specific cluster assignment for each pixel; these assignments then serve as labels to reconstruct the segmented image (Figure 2(d)). In Section 2, we detail the mechanism based on hedonic games (Felipe et al., 2025). Section 3 then evaluates the overlap between the equilibrium partitions produced by the mechanism and the ground-truth foreground coalition (Figure 2(e)). Section 4 concludes with a summary of our contributions and future work.¹

2 HEDONIC MECHANISM FOR COALITION FORMATION

A hedonic game is a naturally decentralized coalition formation game in which an agent’s preference depends strictly on the composition of its own coalition (Aziz and Savani, 2016). A potential game allows unilateral improvements by individual agents to be aligned with the maximization of a global potential function, where local dynamics can be interpreted as hill-climbing a single objective (Monderer and Shapley, 1996).

Felipe et al. (2025) modeled the Constant Potts Model (CPM) (Traag et al., 2011), a quality function known for being a *resolution-limit-free* method (Fortunato and Barthelemy, 2007), as an *additively separable potential hedonic game*. The CPM is decomposed into individual agent utilities (hedonic potentials). This frames the mechanism as a non-cooperative game while remaining aligned with a global quality function, ensuring that selfish agents’ decisions yield stable, cooperative coalitions.

Potential. Each player seeks to belong to the community that maximizes its utility, in which better balances attraction to well-connected neighbors against a penalty for joining large, weakly connected coalitions. For a node v and community C , we define

$$\text{Potential}_v^\gamma(C) = (1 - \gamma) d(v, C) - \gamma \bar{d}(v, C) \quad (1)$$

where $d(v, C)$ denotes the degree of v in community C , while $\bar{d}(v, C)$ is the number of non-neighbors in community C , therefore $|C| = 1 + d(v, C) + \bar{d}(v, C)$ is the number of nodes in C . The parameter $\gamma \in [0, 1]$ controls the trade-off between cohesion and coalition size: small γ favors larger cohesive regions, while larger γ penalizes large communities and promotes fragmentation into smaller coalitions (Figure 1).

Equilibrium. An *equilibrium* is a stable partition $\pi = \{C_1, \dots, C_K\}$ where no agent has an incentive to change their community. This state is reached when every node is *locally stable*, meaning its current community C_{σ_v} provides a potential greater than or equal to any other community C_k :

$$\text{Potential}_v^\gamma(C_{\sigma_v}) \geq \text{Potential}_v^\gamma(C_k) \quad \forall k \neq \sigma_v. \quad (2)$$

A partition is considered a solution to the community detection problem if it satisfies two conditions:

- **Internal Stability:** No node wants to leave its current community.
- **External Stability:** No node wants to join a different existing community.

¹We detail our graph construction in Appendix A. While it is impactful for performance, our mechanism is agnostic to the specific construction method as long as the input is a weighted graph; thus, evaluating alternatives remains future work. Figs. 2(b) and 2(c) are downsampled versions of Fig. 2(a) for visual clarity.

Algorithm 1: Hedonic optimization: The algorithm terminates at a locally stable equilibrium.

Input : Weighted Graph $G = (V, E, w)$, resolution γ , partition $\pi^{(0)}$
Output: Equilibrium partition $\pi = \{C_1, \dots, C_K\}$

```

1 if  $\pi^{(0)}$  not provided then
2   | Assign each node to its own community           ▷ Initialize a singleton partition
3 change  $\leftarrow$  true                               ▷ Activate the main improvement loop
4 while change do
5   |                               ▷ Iterate while at least one beneficial node move occurs
6   | change  $\leftarrow$  false                               ▷ Clear the change flag
7   | foreach node  $v \in V$  do
8     |  $\sigma_v \leftarrow$  current community of  $v$            ▷ Retrieve current community  $\sigma_v$ 
9     |  $\sigma^* \leftarrow \arg \max_C \text{Potential}_v^\gamma(C)$        ▷ get community maximizing potential
10    | if  $\text{Potential}_v^\gamma(\sigma^*) > \text{Potential}_v^\gamma(\sigma_v)$  then
11      |                               ▷ Check for strict potential improvement
12      |   Move  $v$  to  $\sigma^*$                                ▷ Reassign the node's community
13      |   change  $\leftarrow$  true                               ▷ Mark change occurred to force another pass

```

In this state, each node v is assigned to a community σ_v that maximizes its individual utility $\sigma_v \in \arg \max_k \text{Potential}_v^\gamma(C_k)$. Movement only occurs if a change offers a **strictly higher** utility. If multiple communities provide the same maximum utility, the node remains in its current community.

Algorithm 1 outlines the hedonic game mechanism,² which relies on a potential function bounded by $2|V|^2$. Given a rational resolution parameter $\gamma = b/\kappa$, every improving move increases the potential by at least $1/\kappa$, guaranteeing convergence in $O(\kappa \cdot |V|^2)$ steps (Felipe et al., 2025).

3 RESULTS

To quantify how γ shapes equilibrium partitions and yields meaningful segmentations, we evaluate the converged partitions using two post-hoc accuracy metrics inspired by Alpert et al. (2007). For each image, we select one binary ground-truth (GT), denoted by Y , where $Y \in \{0, 1\}^{H \times W}$:

- F_1^{single} (**Dominant-Coalition Accuracy**): Evaluates the F_1 score of the *single* community $C_k \in \pi$ that maximizes the F_1 score relative to Y ;
- F_1^{union} (**Recoverable-Union Accuracy**): Evaluates the F_1 score of the *subset* of communities $S \subseteq \{C_1, \dots, C_K\}$ whose union maximizes the F_1 score relative to Y .

F_1 is the harmonic mean of precision and recall (Christen et al., 2023). Specifically, F_1^{single} measures the emergence of a cohesive foreground, while F_1^{union} assesses whether the foreground object, even if fragmented, remains “recoverable” from the equilibrium structure. Formal definitions, algorithmic details, and additional properties of F_1^{single} and F_1^{union} are provided in Appendix F.

We use the *Weizmann Segmentation Evaluation Database* (Alpert et al., 2007) to obtain images with known ground truth, which is used exclusively at evaluation time. Note that we restrict our analysis to the single-object subset (100 natural images, 3 human ground-truth masks per image) and leave the two-object subset for future work. Experiments can be reproduced at: <https://github.com/henriquepedro1991/hedonic-games-to-image-segmentation>.

Resolution Design. We extend the approach of Avrachenkov et al. (2018)—setting the resolution as the graph’s edge density—by proposing a scaling approach to evaluate varying density ratios:

$$\gamma = \frac{\text{density}(G)}{c}, \quad \text{density}(G) = \frac{2|E|}{|V|(|V| - 1)},$$

²Algorithm 1 presents a simplified version of the optimization process to illustrate the underlying mechanics. In practice, scanning all nodes (Line 6) results in many “ignorable checks” that do not yield strict improvements. To achieve high performance, we utilize the `community_leiden` method (Traag et al., 2019) (of the `igraph` Python library) optimizing the CPM (Traag et al., 2011), which serves as the core of our pipeline.

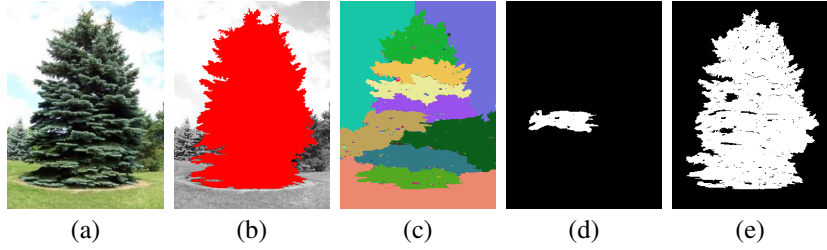


Figure 3: Projections from a multi-community partition. (a) Original image. (b) Binary ground-truth mask. (c) Equilibrium partition by hedonic mechanism. (d) Best single community selected by F_1^{single} at $\gamma = 7.63 \times 10^{-6}$. (e) Best subset of communities selected by F_1^{union} at $\gamma = 2.96 \times 10^{-5}$.

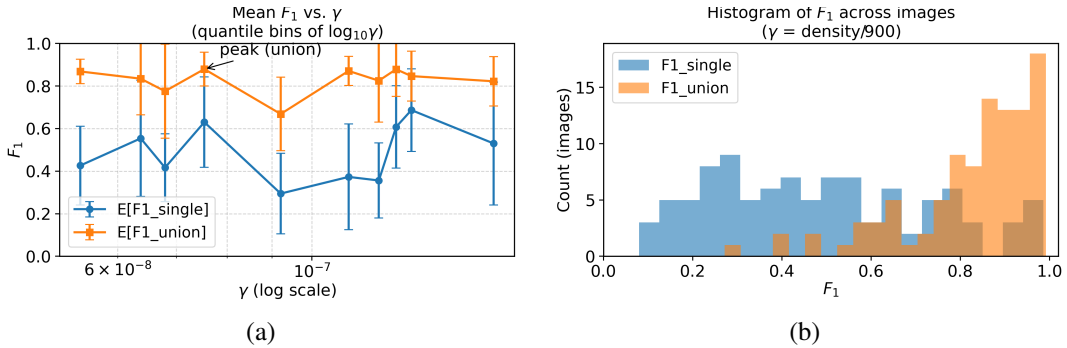


Figure 4: (a) Mean F_1^{single} and F_1^{union} as a function of γ (induced by $\text{density}(G)/900$). (b) Global distributions of F_1^{single} and F_1^{union} over 100 images after selecting the best GT per image.

where c is a fixed constant. This normalization allows γ to act as a consistent local decision threshold across graphs of varying sparsity.

Figure 4 highlights the key insights from our experiments (see Appendix B for additional details). Our numerical results identified $c = 900$ as the optimal value to place most instances in the fragmented-but-recoverable regime (Figure 4(a)). Across all images, we obtain $\mathbb{E}[F_1^{\text{union}}] \approx 0.828$ (median ≈ 0.868) and $\mathbb{E}[F_1^{\text{single}}] \approx 0.488$, with an average gap $\mathbb{E}[F_1^{\text{union}} - F_1^{\text{single}}] \approx 0.340$ (cf. Figure 4(b)). The significant average performance gap suggests that many apparent segmentation failures are actually fragmented, yet entirely recoverable, equilibria. Indeed, the partition produced by the hedonic mechanism often contains the object, but distributed across several coalitions.

4 CONCLUSION

We proposed image segmentation as an interpretable testbed for studying equilibrium in hedonic games. This spatial and visual setting makes equilibrium structures directly *inspectable*, providing an intuitive way to analyze how coalition mechanisms behave. In particular, it highlights how a resolution parameter reshapes equilibrium geometry in a visually grounded domain.

Our results demonstrate that a density-normalized rule, $\gamma = \text{density}(G)/c$, places most instances in favorable regimes by successfully preventing extreme over- or under-fragmentation (Appendix C). Appendix D reveals that a low $F_1^{\text{union}} - F_1^{\text{single}}$ gap indicates either mutual success for cohesive structures or intrinsic failure for detailed objects. Appendix E confirms the robustness of the mechanism, demonstrating no difference in equilibrium accuracy whether initializing as a fragmenting grand coalition or as merging isolated nodes. Finally, Appendix F formalizes the computation of these binary projections and establishes the theoretical recoverability limits of F_1^{union} .

Future work includes evaluating alternative graph constructions and the Weizmann two-object subset. We also aim to investigate the relationship between accuracy and resolution, focusing on merging fragmented but recoverable coalitions to reduce the gap between F_1^{single} and F_1^{union} .

REFERENCES

- Sharon Alpert, Meirav Galun, Ronen Basri, and Achi Brandt. Image segmentation by probabilistic bottom-up aggregation and CUE integration. In *Proceedings of the IEEE Conference on Computer Vision and Pattern Recognition (CVPR)*, June 2007.
- Konstantin E Avrachenkov, Aleksei Y Kondratev, Vladimir V Mazalov, and Dmytro G Rubanov. Network partitioning algorithms as cooperative games. *Computational Social Networks*, 5(1), 2018. doi: 10.1186/s40649-018-0059-5.
- Haris Aziz and Rahul Savani. Hedonic games. In *Handbook of Computational Social Choice*, pages 356–376. Cambridge University Press, Cambridge, 2016.
- Anna Bogomolnaia and Matthew O Jackson. The stability of hedonic coalition structures. *Games and Economic Behavior*, 38(2):201–230, 2002.
- Joao Carreira and Cristian Sminchisescu. CPMC: Automatic object segmentation using constrained parametric min-cuts. *IEEE Transactions on Pattern Analysis and Machine Intelligence*, 34(7):1312–1328, 2011.
- Peter Christen, David J Hand, and Nishadi Kirielle. A review of the f-measure: its history, properties, criticism, and alternatives. *ACM Computing Surveys*, 56(3):1–24, 2023.
- Lucas Lopes Felipe, Konstantin Avrachenkov, and Daniel Sadoc Menasché. From Leiden to Pleasure Island: The Constant Potts Model for community detection as a hedonic game. *Physica A: Statistical Mechanics and its Applications*, page 130989, 2025.
- Santo Fortunato and Marc Barthelemy. Resolution limit in community detection. *Proceedings of the national academy of sciences*, 104(1):36–41, 2007.
- Galun, Sharon, Basri, and Brandt. Texture segmentation by multiscale aggregation of filter responses and shape elements. In *Proceedings Ninth IEEE International Conference on Computer Vision*, pages 716–723. IEEE, 2003.
- Himanshu Mittal, Avinash Chandra Pandey, Mukesh Saraswat, Sumit Kumar, Raju Pal, and Garv Modwel. A comprehensive survey of image segmentation: clustering methods, performance parameters, and benchmark datasets. *Multimedia Tools and Applications*, 81(24):35001–35026, 2022.
- Dov Monderer and Lloyd S Shapley. Potential games. *Games and economic behavior*, 14(1):124–143, 1996.
- Jianbo Shi and Jitendra Malik. Normalized cuts and image segmentation. In *Proceedings of the IEEE Conference on Computer Vision and Pattern Recognition (CVPR)*, pages 731–737. IEEE, 1997.
- Vincent A Traag, Paul Van Dooren, and Yurii Nesterov. Narrow scope for resolution-limit-free community detection. *Physical Review E*, 84(1):016114, 2011.
- Vincent A Traag, Ludo Waltman, and Nees Jan van Eck. From Louvain to Leiden: guaranteeing well-connected communities. *Scientific Reports*, 9(1):5233, 2019.

A PIXEL-GRAPH CONSTRUCTION

Recall that our pipeline is given by Figure 5. Next, we focus on the pixel-graph construction (Image \rightarrow Graph). Each image is converted into an undirected weighted pixel graph $G = (V, E, w)$, where each pixel corresponds to a node and candidate edges connect spatially adjacent pixels under an 8-neighborhood system, including horizontal, vertical, and diagonal neighbors.

Rather than using a binary adjacency rule based on exact intensity agreement, we assign each neighboring pair (u, v) a continuous affinity weight that combines color similarity and boundary evidence. Let $I(u) \in [0, 255]^3$ denote the RGB vector at pixel u , and let $B : \Omega \rightarrow [0, 1]$ be a normalized edge map used as a proxy for boundary probability. For each adjacent pair (u, v) , we define

$$w_{uv} = \exp\left(-\frac{\|I(u) - I(v)\|_2^2}{\sigma_{\text{color}}^2}\right) \exp\left(-\frac{\max\{B(u), B(v)\}}{\sigma_{\text{edge}}^2}\right). \quad (3)$$

In our implementation, B is obtained from a normalized Canny edge map, used as a lightweight proxy for contour strength rather than the original gPb detector. Thus, affinities are high when adjacent pixels have similar RGB values and low when they lie near strong image boundaries. Edges with very small affinity are discarded, yielding a sparse local graph.

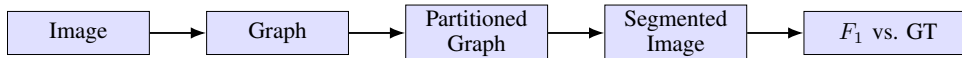


Figure 5: Diagnostic pipeline: image \rightarrow graph \rightarrow hedonic partition \rightarrow binary projection and evaluation.

This construction biases the graph toward forming coalitions inside locally homogeneous color regions while reducing affinity across strong visual discontinuities. Consequently, the subsequent community-detection hedonic game is encouraged to group pixels within coherent regions and to place coalition boundaries near salient contours.

Although this construction is inspired by pairwise affinity ideas used in graph-based segmentation, it is not a full CPMC (Carreira and Sminchisescu, 2011) formulation: unlike CPMC, we do not solve seeded constrained parametric min-cut problems. Instead, we use the resulting weighted pixel graph as input to the hedonic optimization described in Section 11.

Note that for the qualitative visualizations in Fig. 2(b)-(c), the graphs were constructed using a downsampled version of the original image to ensure the nodes and edges remain discernible for the reader. However, all quantitative experiments and results reported in Section 3 were conducted using the original pixel-level resolution of the Weizmann dataset without any pre-processing or scaling.

B NUMERICAL REPORT

We evaluate the proposed diagnostic framework on the Weizmann single-object subset, focusing on how the resolution parameter γ shapes equilibrium structure in hedonic coalition formation and how this structure is reflected by the complementary scores F_1^{single} and F_1^{union} . Our goal is to characterize equilibrium regimes and failure modes of the mechanism.

Protocol and Ground-Truth Selection. Each image has three human ground-truth (GT) masks. For each GT we compute F_1^{single} and F_1^{union} , and then select, per image, the GT that maximizes F_1^{union} . We found low sensitivity to the choice of ground truth, as reported in Appendix E. Unless otherwise stated, we use the density-normalized resolution $\gamma = \text{density}(G)/900$. Figure 4(a) reports the mean F_1^{single} and F_1^{union} over 100 images as a function of γ , while Figure 4(b) shows their global distributions.

Regime Transitions. As shown in Figure 4(a), for $\gamma < 10^{-7}$, F_1^{single} and F_1^{union} are close on average, indicating a *cohesive regime* in which the foreground typically appears as a single dominant coalition. As γ increases, the two curves separate: F_1^{single} decreases markedly, while F_1^{union} remains comparatively high over a broad interval. This gap characterizes a *fragmented but recoverable regime*, where the foreground is present in the partition but distributed across multiple coalitions. For larger γ , the behavior becomes more heterogeneous across images: F_1^{union} often remains high, while F_1^{single} becomes non-monotone, showing a partial rebound followed by a mild decline. This pattern is consistent with highly fragmented partitions in which the foreground can still be recovered by aggregating multiple coalitions, even though it rarely emerges as a single dominant one. Operationally, the pair $(F_1^{\text{single}}, F_1^{\text{union}})$ distinguishes three broad situations: cohesive success (both high), recoverable fragmentation (large gap), and intrinsic failure (both low).

Average Performance. Across all images, we obtain $\mathbb{E}[F_1^{\text{union}}] \approx 0.828$ (median ≈ 0.868) and $\mathbb{E}[F_1^{\text{single}}] \approx 0.488$, with an average gap $\mathbb{E}[F_1^{\text{union}} - F_1^{\text{single}}] \approx 0.340$ (cf. Figure 4(b)). This large systematic gap shows that many apparent failures under a dominant-coalition criterion arise from the difficulty of recomposing fragmented equilibria into a single binary mask. Qualitative extremes further clarify this interpretation: Appendix D contrasts a peak case, where both projections closely match the object, with a decay case, where even recoverable union cannot recover a good foreground mask.

Robustness to Initialization. We repeat the protocol with two extreme initializations: *singleton* (each node starts alone) and *one-coalition* (all nodes start together), and observe negligible differences between them (Appendix E). We also analyze fragmentation via the number of communities K : K increases monotonically with γ , and high F_1^{single} occurs mainly at small K , whereas high F_1^{union} appears across a wide range of K . Additional diagnostics are provided in Appendix C. These regimes also suggest distinct failure modes. A large $F_1^{\text{union}} - F_1^{\text{single}}$ gap indicates recoverable fragmentation, where the object is distributed across multiple coalitions. Cases where both scores are low are more consistent with intrinsic failure or background leakage, in which the partition itself does not support accurate figure-ground recovery even under recoverable recomposition.

C FRAGMENTATION DIAGNOSTICS

This appendix provides detailed diagnostics relating fragmentation level, resolution, and performance. We begin by examining how the number of communities K produced by the hedonic optimization varies with the resolution parameter γ , as well as how overall F_1 scores depend on γ .

Figure 6(a) shows K versus γ . While the scatter exhibits substantial dispersion, there is a positive upward trend: larger values of γ are associated, on average, with larger numbers of communities, indicating increasingly fragmented equilibrium partitions.

Figure 6(b) shows F_1 versus γ . The plot suggests that F_1^{union} tends to attain higher and more stable values across the considered range of γ , whereas F_1^{single} is more dispersed and harder to predict. In particular, F_1^{single} typically takes lower values for intermediate values of γ , consistent with a fragmentation regime in which the foreground is split across multiple communities.

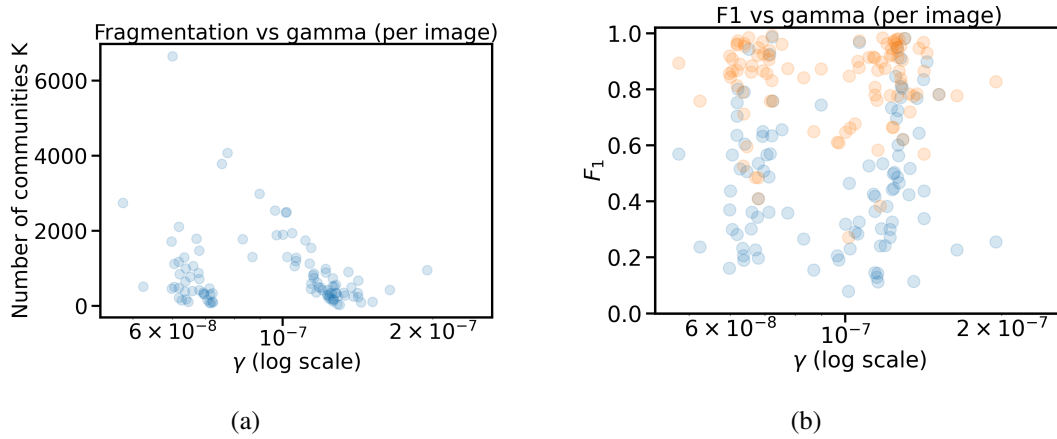


Figure 6: Diagnostics as a function of the resolution parameter γ . (a) Fragmentation K vs. γ . (b) F_1 vs. γ . Orange points correspond to $F_{1,\text{union}}$ and blue points to $F_{1,\text{single}}$.

Next, we relate fragmentation directly to performance. Figure 7 shows F_1 versus the number of communities K . Values of F_1^{single} exhibit substantial dispersion and are strongly concentrated at small K , suggesting that dominant-coalition recovery typically requires low fragmentation and becomes unreliable as fragmentation increases. In contrast, high F_1^{union} values are observed across a wider range of K , indicating that the foreground can remain recoverable even when distributed across many communities.

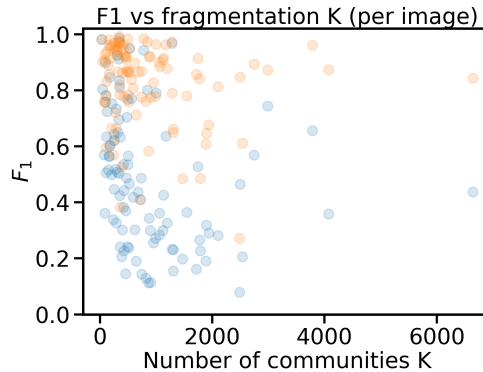


Figure 7: F_1 vs # of communities K . Orange and blue points correspond to $F_{1,\text{union}}$ and $F_{1,\text{single}}$.

Finally, Figure 8 shows the histogram of K over all images. The distribution suggests that the density-normalized choice $\gamma = \text{density}(G)/c$ places a substantial number of instances in an intermediate fragmentation regime, rather than at extreme values of very small or very large K .

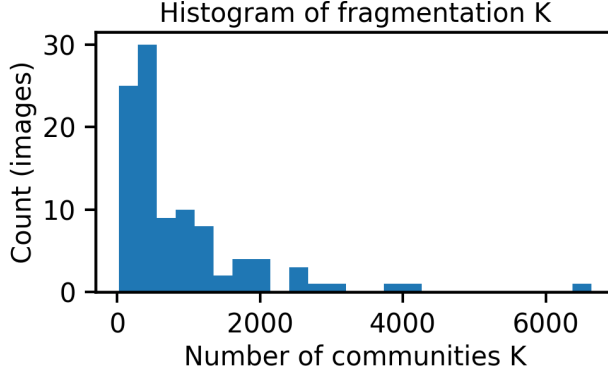


Figure 8: Global distribution of the number of communities K over 100 images.

D QUALITATIVE EXTREMES: PEAK AND DECAY CASES

To complement the aggregate trends reported in Section 3, we present two qualitative extremes that help interpret how the scores F_1^{single} and F_1^{union} arise in practice. We select one *peak* case, corresponding to the image with the highest F_1^{union} in the dataset, and one *decay* case, corresponding to the image with the lowest F_1^{union} .

These examples clarify how the same multi-coalition mechanism can produce either highly recoverable partitions or severe failure under fragmentation and/or background leakage. In both cases, panels (a) and (b) show the original image and the selected ground-truth mask, respectively; panel (c) shows the best single-community projection associated with F_1^{single} , and panel (d) shows the recoverable union used to compute F_1^{union} .

D.1 PEAK CASE

Figure 9 shows a representative case in which the partition aligns very well with the object. The best single coalition already captures most of the foreground, yielding $F_1^{\text{single}} = 0.9863$, and the recoverable union provides only a marginal improvement, reaching $F_1^{\text{union}} = 0.9922$. This is consistent with a cohesive regime in which the object emerges almost entirely as a single dominant coalition.

D.2 DECAY CASE

Figure 10 shows the opposite extreme. Here the partition fails to produce a coalition that matches the object well, giving $F_1^{\text{single}} = 0.0370$. Even after recoverable recombination, the result remains poor, with $F_1^{\text{union}} = 0.2714$. This case is representative of intrinsic failure under severe fragmentation and/or figure-ground mixing: the object is not cleanly represented in the partition, so even an optimistic oracle union cannot recover a high-quality binary mask.

Taken together, these qualitative extremes reinforce the interpretation of the two-score diagnostic. In peak cases, both F_1^{single} and F_1^{union} are high, indicating that the foreground is well represented and largely cohesive in the partition. In decay cases, both scores are low, indicating that the limitation is not merely downstream recombination, but rather the inability of the partition itself to represent the object cleanly under the chosen graph construction and resolution regime.

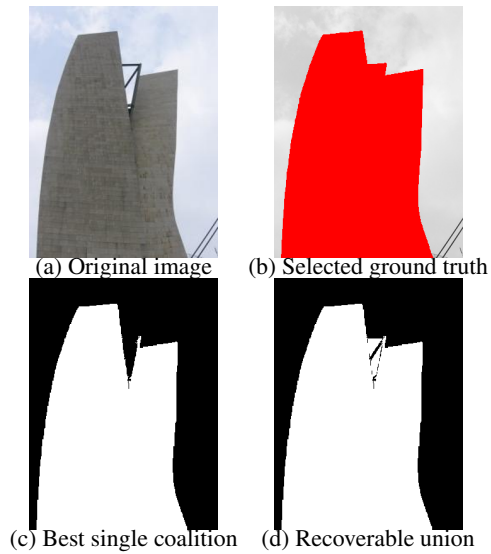


Figure 9: Peak example: the partition aligns closely with the selected ground truth. The best single coalition already attains $F_1^{\text{single}} = 0.9863$, while the recoverable union slightly improves performance to $F_1^{\text{union}} = 0.9922$.

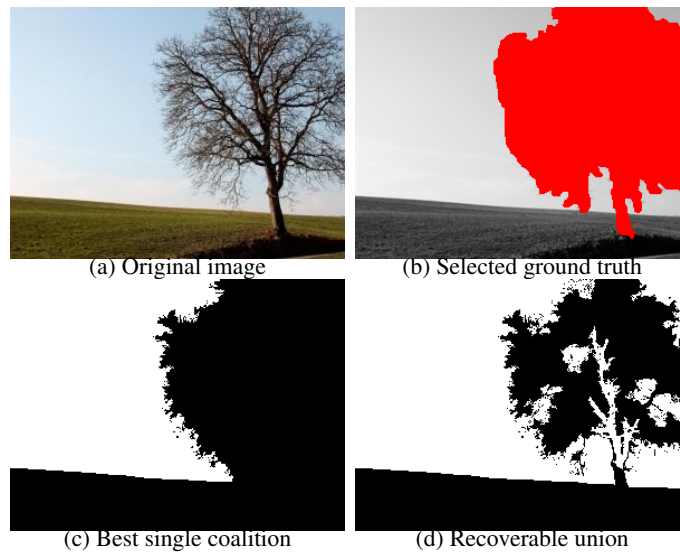


Figure 10: Decay example: the partition exhibits severe failure, with no single coalition capturing the object well and only limited improvement under recoverable union. The scores are $F_1^{\text{single}} = 0.0370$ and $F_1^{\text{union}} = 0.2714$.

E SENSITIVITY TO INITIALIZATION AND TO GROUND TRUTH LABELS

Figure 11 summarizes the F_1 distributions across all images for each ground truth under both initialization strategies. Recall that the dataset provides three ground truth labels. Each column of Figure 11 corresponds to the use of a different label. Each plot reports the distribution over 100 images, with the top row corresponding to F_1^{single} and the bottom row to F_1^{union} . Figure 11a shows the results obtained with singleton initialization (each node starts alone), while Figure 11b reports the one-coalition initialization (all nodes start together). We observe nearly identical distributions across both cases, indicating negligible sensitivity to initialization.

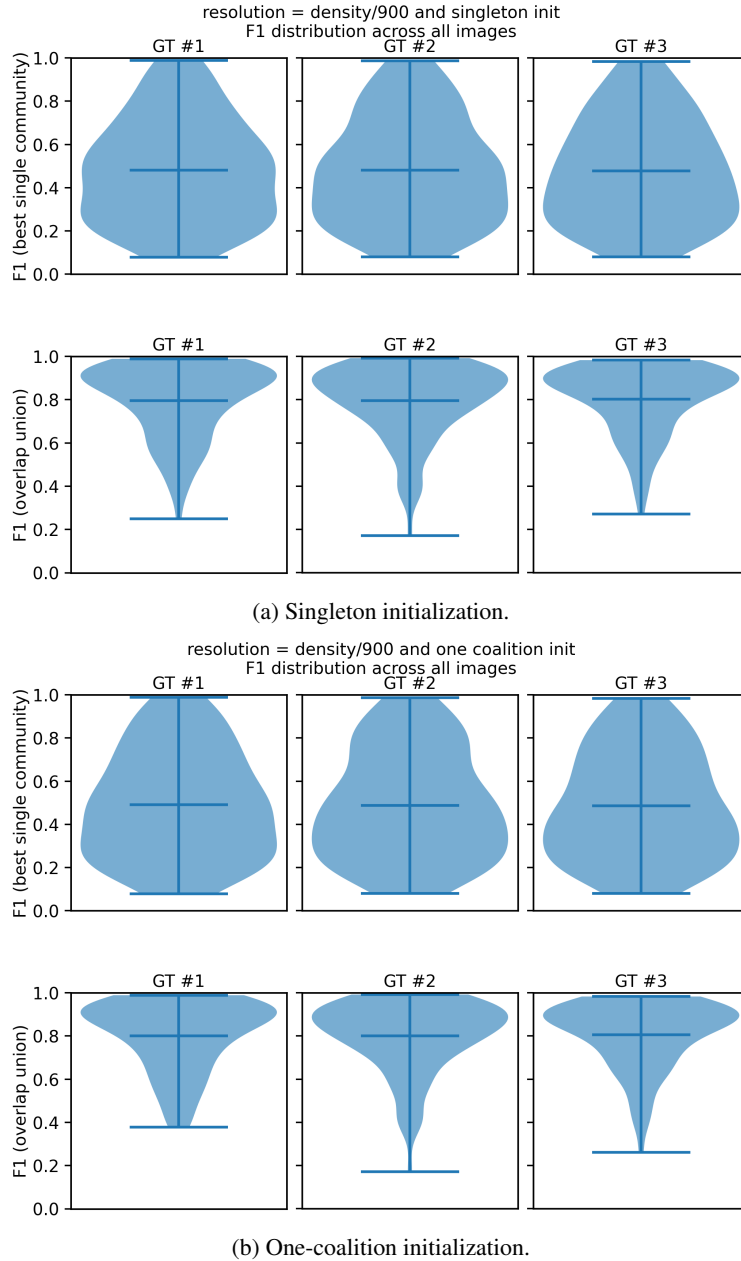


Figure 11: Violin plots over 100 images with $\gamma = \text{density}(G)/900$. In each panel, the top row shows F_1^{single} and the bottom row shows F_1^{union} .

F DETAILS OF BINARY PROJECTIONS AND F_1 COMPUTATION

This appendix provides a detailed mathematical specification of the binary projections F_1^{single} and F_1^{union} , as well as the underlying F_1 measure used throughout the paper.

F_1^{single} (dominant coalition). Let $\mathbf{L} \in \{1, \dots, K\}^{H \times W}$ be the label image. For each community label k , define $\hat{Y}_k(p) = \mathbb{1}[\mathbf{L}(p) = k]$, and set $F_1^{\text{single}}(\Pi) = \max_k F_1(\hat{Y}_k, Y)$. This score measures whether the foreground object emerges as a *single dominant coalition*.

F_1^{union} (recoverable union). Using the ground-truth mask *only at evaluation time*, we construct $\hat{Y}_S(p) = \bigvee_{k \in S} \mathbb{1}[\mathbf{L}(p) = k]$ via a greedy forward pass that initializes S with the label attaining F_1^{single} , orders the remaining communities by their individual $F_1(\hat{Y}_k, Y)$ scores, and then scans this list once, adding communities while their inclusion increases the current F_1 (with a cap on merged labels). The resulting score $F_1^{\text{union}}(\Pi) = F_1(\hat{Y}_S, Y)$ upper-bounds how well the foreground can be recovered from the partition.

F.1 BINARY MASKS AND PIXEL SETS

Let the image domain be $\Omega = \{1, \dots, H\} \times \{1, \dots, W\}$. The ground-truth foreground mask is

$$Y(p) \in \{0, 1\}, \quad p \in \Omega,$$

and the predicted community labeling is

$$\mathbf{L}(p) \in \{1, \dots, K\}.$$

For any binary mask $B : \Omega \rightarrow \{0, 1\}$, define the corresponding foreground pixel set

$$\mathcal{B} = \{p \in \Omega : B(p) = 1\}, \quad \mathcal{Y} = \{p \in \Omega : Y(p) = 1\}.$$

F.2 PRECISION, RECALL, AND F_1

Given a predicted mask B , we define

$$\text{Precision}(B, Y) = \frac{|\mathcal{B} \cap \mathcal{Y}|}{|\mathcal{B}|}, \quad \text{Recall}(B, Y) = \frac{|\mathcal{B} \cap \mathcal{Y}|}{|\mathcal{Y}|}.$$

The F_1 score is the harmonic mean of precision and recall:

$$F_1(B, Y) = \frac{2 \text{Precision}(B, Y) \text{Recall}(B, Y)}{\text{Precision}(B, Y) + \text{Recall}(B, Y)} = \frac{2|\mathcal{B} \cap \mathcal{Y}|}{|\mathcal{B}| + |\mathcal{Y}|}.$$

F.3 F_1^{SINGLE} : DOMINANT-COALITION PROJECTION

For each community label k , we define the induced binary mask

$$\hat{Y}_k(p) = \mathbb{1}[\mathbf{L}(p) = k], \quad \mathcal{C}_k = \{p : \mathbf{L}(p) = k\}.$$

The dominant-coalition score is

$$F_1^{\text{single}}(\Pi) = \max_{k \in \{1, \dots, K\}} F_1(\hat{Y}_k, Y) = \max_k \frac{2|\mathcal{C}_k \cap \mathcal{Y}|}{|\mathcal{C}_k| + |\mathcal{Y}|}.$$

Thus, F_1^{single} measures whether there exists a *single* community whose pixels align well with the foreground object.

F.4 F_1^{UNION} : RECOVERABLE UNION

For any subset of labels $S \subseteq \{1, \dots, K\}$, define the union mask

$$\hat{Y}_S(p) = \bigvee_{k \in S} \mathbb{1}[\mathbf{L}(p) = k], \quad \mathcal{U}_S = \bigcup_{k \in S} \mathcal{C}_k.$$

The corresponding F_1 score is

$$F_1(\hat{Y}_S, Y) = \frac{2|\mathcal{U}_S \cap \mathcal{Y}|}{|\mathcal{U}_S| + |\mathcal{Y}|}.$$

We construct S by a forward selection procedure that uses ground truth only at evaluation time:

1. Compute $F_1(\hat{Y}_k, Y)$ for all labels k and sort labels in decreasing order of this score.
2. Initialize S with the label attaining $F_{1,\text{single}}(\Pi)$.
3. Scan the sorted list once and add a label k to S while $F_1(\hat{Y}_{S \cup \{k\}}, Y) > F_1(\hat{Y}_S, Y)$.

The resulting score is

$$F_1^{\text{union}}(\Pi) = F_1(\hat{Y}_S, Y).$$

F_1^{union} approximates

$$\max_{S \subseteq \{1, \dots, K\}} F_1(\hat{Y}_S, Y),$$

which is the best achievable binary reconstruction from the given partition.

F.5 GREEDY FORWARD PROCEDURE FOR COMPUTING F_1^{UNION}

Algorithm 2 summarizes the greedy forward procedure used throughout the paper to compute F_1^{union} . Starting from the best single community (the one attaining F_1^{single}), the method scans the remaining communities in decreasing order of their individual F_1 scores and adds a label only when its inclusion strictly improves the current union score.

Algorithm 2: Greedy forward union used to compute F_1^{union} .

Input : Partition $\Pi = \{C_1, \dots, C_K\}$ (equivalently, label image \mathbf{L})

Binary ground-truth mask $Y \in \{0, 1\}^{H \times W}$

Optional cap L_{\max} on the number of merged labels

Output: Selected label set S and score $F_1^{\text{union}}(\Pi) = F_1(\hat{Y}_S, Y)$

- 1 Compute $F_1(\hat{Y}_k, Y)$ for all $k = 1, \dots, K$
 - 2 Let $k^* \in \arg \max_k F_1(\hat{Y}_k, Y)$ and initialize $S \leftarrow \{k^*\}$
 - 3 Order the remaining labels $k \neq k^*$ by decreasing $F_1(\hat{Y}_k, Y)$
 - 4 **foreach** label k in the ordered list **do**
 - 5 **if** L_{\max} is specified and $|S| = L_{\max}$ **then**
 - 6 **break**
 - 7 **if** $F_1(\hat{Y}_{S \cup \{k\}}, Y) > F_1(\hat{Y}_S, Y)$ **then**
 - 8 **break** $S \leftarrow S \cup \{k\}$
 - 9 **return** S and $F_1^{\text{union}}(\Pi) = F_1(\hat{Y}_S, Y)$
-

F.6 ALTERNATIVE RECOVERABLE-UNION VARIANT

For completeness, Algorithm 3 presents a simple alternative union rule based on per-community overlap with the ground truth. Unlike the greedy forward procedure used for F_1^{union} , this variant

evaluates each community independently and selects all labels whose individual overlap score exceeds a fixed threshold. We do not use this rule in the main experiments; it is included only to illustrate that multiple oracle-style unions are possible.

Algorithm 3: Threshold-based recoverable union as an alternative oracle variant.

Input : Partition $\Pi = \{C_1, \dots, C_K\}$
 Binary ground-truth mask $Y \in \{0, 1\}^{H \times W}$
 Overlap threshold $\tau \in [0, 1]$
Output: Selected label set S and union mask \hat{Y}_S

- 1 $S \leftarrow \emptyset$
- 2 **for** $k \in \{1, \dots, K\}$ **do**
- 3 Compute the individual overlap score of C_k with Y
- 4 **if** $F_1(\hat{Y}_k, Y) > \tau$ **then**
- 5 $S \leftarrow S \cup \{k\}$
- 6 **return** S and $\hat{Y}_S(p) = \bigvee_{k \in S} \mathbb{1}[\mathbf{L}(p) = k]$

F.7 INTERPRETING THE GAP BETWEEN F_1^{SINGLE} AND F_1^{UNION}

- Small gap: foreground appears largely as a single coalition.
- Large gap: foreground is distributed across several communities (fragmentation).
- Both small: intrinsic failure (object not represented well in partition).

Hence, the pair $(F_1^{\text{single}}, F_1^{\text{union}})$ disentangles failures due to coalition structure from failures due to downstream binary projection.

F.8 TOY EXAMPLE: DOMINANT COALITION VS. RECOVERABLE UNION

Consider an image with $|\mathcal{Y}| = 100$ foreground pixels and three communities C_1, C_2, C_3 with the following *spatial overlaps*:

$$\begin{aligned} |C_1| &= 40, & |C_2| &= 35, & |C_3| &= 50, \\ |C_1 \cap \mathcal{Y}| &= 30, & |C_2 \cap \mathcal{Y}| &= 25, & |C_3 \cap \mathcal{Y}| &= 10. \end{aligned}$$

Single-community scores.

$$F_1(C_1) = \frac{2 \cdot 30}{40 + 100} = 0.43, \quad F_1(C_2) = \frac{2 \cdot 25}{35 + 100} = 0.37, \quad F_1(C_3) = \frac{2 \cdot 10}{50 + 100} = 0.13.$$

Thus,

$$F_1^{\text{single}} = 0.43.$$

Union of communities. Let $S = \{1, 2\}$. Then

$$|\mathcal{U}_S| = 75, \quad |\mathcal{U}_S \cap \mathcal{Y}| = 55.$$

$$F_1(\hat{Y}_S, Y) = \frac{2 \cdot 55}{75 + 100} = 0.63.$$

Hence,

$$F_1^{\text{union}} = 0.63 > F_1^{\text{single}}.$$

This example illustrates a fragmented-but-recoverable situation: no single community captures the object well, yet combining two communities yields good foreground reconstruction.

F.9 RELATION TO FIGURE 3

The behavior visualized in Figure 3 corresponds to the label selection described in this section. In Figure 3(c), F_1^{single} selects the single community with the highest individual F_1 score. The F_1^{union} mask is formed by the greedy forward union described above, which aggregates communities whose addition improves the current F_1 score. This captures the entire object by aggregating the multiple fragments that individually correspond to parts of the foreground (e.g., $S = \{1, 2\}$ in the toy example), without requiring an iterative optimization search.

F.10 WHEN THE RECOVERABLE-UNION CAN BE SUBOPTIMAL

The recoverable-union procedure is a heuristic for approximating

$$\max_{S \subseteq \{1, \dots, K\}} F_1(\hat{Y}_S, Y),$$

which is combinatorial in K . As with many subset-selection methods, optimality is not guaranteed.

A typical failure mode occurs when two communities are individually weak predictors of the foreground but jointly complementary. For example, two communities may each cover disjoint halves of the object while also containing substantial background. Individually, neither improves F_1 enough to be selected, but together they would yield a strong score.

Formally, the forward selection can fail when

$$F_1(\hat{Y}_{\{i\}}, Y) \leq F_1(\hat{Y}_S, Y) \quad \text{and} \quad F_1(\hat{Y}_{\{j\}}, Y) \leq F_1(\hat{Y}_S, Y),$$

but

$$F_1(\hat{Y}_{S \cup \{i, j\}}, Y) \gg F_1(\hat{Y}_S, Y).$$

Exact subset search would recover $\{i, j\}$, while forward selection would stop early.

In practice, this pathology is rare in our setting because foreground fragments tend to have nontrivial individual *spatial overlap* with the object, making them attractive early additions.

F.11 HOW LARGE CAN THE GAP $F_1^{\text{UNION}} - F_1^{\text{SINGLE}}$ BE?

In the worst case, the gap between F_1^{union} and F_1^{single} can be arbitrarily large.

Consider an object split evenly across M disjoint communities, each containing exactly $\frac{1}{M}|\mathcal{Y}|$ foreground pixels and no background. Then, for each community k ,

$$F_1(\hat{Y}_{\{k\}}, Y) = \frac{2 \cdot \frac{1}{M}|\mathcal{Y}|}{\frac{1}{M}|\mathcal{Y}| + |\mathcal{Y}|} = \frac{2}{M+1}.$$

Thus,

$$F_1^{\text{single}} = \frac{2}{M+1}.$$

If we union all M communities, we recover the full object:

$$F_1(\hat{Y}_{\{1, \dots, M\}}, Y) = 1, \quad F_1^{\text{union}} = 1.$$

Hence,

$$F_1^{\text{union}} - F_1^{\text{single}} = 1 - \frac{2}{M+1},$$

which approaches 1 as $M \rightarrow \infty$.

This construction demonstrates that a very low F_1^{single} does not necessarily indicate failure of coalition formation: it may simply reflect extreme fragmentation of an otherwise perfectly recoverable object.

In contrast, small gaps between F_1^{single} and F_1^{union} indicate that even multi-coalition recomposition cannot recover the foreground, pointing to intrinsic failure modes such as background leakage or poor boundary placement.

The pathological lower bound for F_1^{single} , under perfect recoverability, is formalized through the following proposition:

Proposition 1 (Arbitrarily small F_1^{single} with $F_1^{\text{union}} = 1$). *For any integer $M \geq 1$, there exists a partition $\Pi = \{C_1, \dots, C_M\}$ and a binary ground-truth mask Y such that*

$$F_1^{\text{union}}(\Pi) = 1 \quad \text{and} \quad F_1^{\text{single}}(\Pi) = \frac{2}{M+1}.$$

Consequently,

$$F_1^{\text{union}}(\Pi) - F_1^{\text{single}}(\Pi) = 1 - \frac{2}{M+1},$$

which can be made arbitrarily close to 1 by taking M large.

Proof sketch. Let Y contain $|\mathcal{Y}|$ foreground pixels. Construct M disjoint communities C_1, \dots, C_M such that each C_k contains exactly $|\mathcal{Y}|/M$ foreground pixels and no background pixels. Then for every k ,

$$\text{TP}_k = \frac{|\mathcal{Y}|}{M}, \quad \text{FP}_k = 0, \quad \text{FN}_k = |\mathcal{Y}| - \frac{|\mathcal{Y}|}{M}.$$

Substituting into the F_1 identity $F_1 = \frac{2\text{TP}}{2\text{TP} + \text{FP} + \text{FN}}$ gives $F_1(\hat{Y}_{\{k\}}, Y) = \frac{2}{M+1}$, hence $F_1^{\text{single}}(\Pi) = \frac{2}{M+1}$. Moreover, the union $\hat{Y}_{\{1, \dots, M\}}$ equals Y , so $F_1(\hat{Y}_{\{1, \dots, M\}}, Y) = 1$. Since F_1^{union} is defined by a union-based projection, $F_1^{\text{union}}(\Pi) = 1$. \square